

Brightness of micronozzle helium source

D. P. DePonte, S. D. Kevan, and F. S. Patton

Physics Department, University of Oregon, Eugene, Oregon 97403-1274

(Received 17 November 2005; accepted 31 March 2006; published online 12 May 2006)

We have measured the brightness of several helium free jet sources. Five converging nozzles with diameters between 0.6 and 5 μm , and three tube nozzles with diameters between 2 and 10 μm were studied at stagnation temperatures of 77 and 300 K and at stagnation pressures depending on nozzle size from 350 to 17000 kPa. Smaller nozzles produced higher brightness beams with values approaching $10^{28} (\text{s sr m}^2)^{-1}$. At low-temperature quantum effects on the helium collision cross section significantly decreased the source brightness. We explore the possibility of producing even higher brightness sources with smaller diameter. © 2006 American Institute of Physics.

[DOI: [10.1063/1.2198813](https://doi.org/10.1063/1.2198813)]

I. INTRODUCTION

Since the inception of gas sources based on the free jet expansion from a nozzle, there has been a great deal of theoretical and experimental work done to characterize the velocity distribution in molecular beams. Parallel speed ratio S is a measure of velocity spread along the streamlines and in the past^{1,2} has been the primary area of study as it determines energy resolution for a variety of scattering applications. Helium beams can be made with very high S , which has made He a useful probe of surface structure, lattice dynamics, and diffusion.³ An alternative way to achieve high-energy resolution, more likely offering a different regime in energy resolution, may be through dynamic scattering techniques similar to those already employed for collimated light sources.⁴ Dynamic atom scattering (DAS) would require a high degree of transverse coherence across the entire beam width and so a good understanding of the transverse velocity distribution is needed. Controlling the transverse coherence of thermal wavelength atom beams is also important in areas closely related to emerging applications of coherent x-ray beams such as interferometry, speckle metrology, and diffractive imaging.⁵

The requirement of transverse coherence for DAS necessitates working with a beam of high brightness. Brightness B may be defined as the intensity per unit area of the source, (particles/s sr m^2), and is a conserved quantity for loss-free propagation. If we defined the transverse coherence solid angle Ω_c by the maximum angular separation over which the field is significantly correlated, then Ω_c is a function of de Broglie wavelength and source area A ⁶

$$\Omega_c = 0.06 \frac{\lambda^2}{A}. \quad (1)$$

The incident scattering flux available for DAS is the coherent flux defined by flux into solid angle Ω_c and average brightness \bar{B} ,

$$F_c = I_0 \Omega_c = 0.06 \bar{B} \lambda^2. \quad (2)$$

Equation (2) indicates that a bright beam rather than an intense beam is desired to optimize transverse coherent flux. Simple scaling arguments imply that small nozzle diameters should produce higher brightness beams and so we have examined micronozzles having diameters as small as 0.63 μm .

It has long been known⁷ that velocity-randomizing collisions downstream from the nozzle produce an effective source area that is larger than the nozzle opening. This larger area determines the brightness of the source and is a primary focus of this work. A virtual source radius r_v or the equivalent such as perpendicular Mach number or perpendicular temperature T_\perp have been studied to describe the perpendicular velocity distribution. The earliest experimental⁸ and theoretical⁹ work described the axial dependence of the perpendicular velocity distribution. Despite some initial apparent contradiction between theory and experiment, this was within a decade was fairly well understood.¹⁰ Later studies more carefully studied the asymptotic behavior of r_v along with deviations from a single Gaussian source^{11,12} and later even deviations form a two-Gaussian description.^{13–15}

This article expands the range of nozzle size for which perpendicular velocity spread has been studied. We include data for a range of expansion strength in which the effects of quantum mechanics on the He–He scattering cross section is large. We compare our results to existing models and analyze our results in terms of the source brightness for the purpose of determining the transverse coherent flux available for DAS or related coherence-based experiments.

II. VIRTUAL SOURCE IN THE SUDDEN FREEZE MODEL

A. Size

A good deal of the theoretical and experimental information available on virtual source size r_v is due to the work of Biejerinck and co-workers in the 1970's and 1980's at the Eindhoven University of Technology in The Netherlands.^{11,12,14,15} In the following, scaling arguments for the dependence of r_v on pressure, temperature, and nozzle

diameter will be reviewed to gain insight into source brightness. For a more detailed model of virtual source size, see Beijerinck and Verster.¹²

A simple, commonly used description of a free jet expansion is given by the sudden freeze model. This model divides the expansion into two regions. In the continuum or isentropic region close to the nozzle, the velocity distribution is described by a single temperature $T_{\perp}=T_{\parallel}=T$ for which equipartition of energy requires

$$T \propto T_0 \left(\frac{D_n}{z} \right)^{4/3} \quad \{z \leq z_f\}, \quad (3)$$

where z is axial distance from the nozzle, d is the nozzle diameter, and z_f the axial distance from the nozzle to the imaginary “freezing” boundary. Beyond z_f is located the free molecular flow region, in which parallel and perpendicular temperatures are assumed to be decoupled so that the system is no longer locally in thermal equilibrium. Without collisions, parallel velocity distribution cannot change and so is said to be “frozen in,” while the perpendicular temperature continues to decrease,

$$\left. \begin{aligned} T_{\perp} &\propto T_0 \left(\frac{d}{z} \right)^2 \\ T_{\parallel} &\propto T_0 S_{\infty}^{-2} \end{aligned} \right\} \quad \{z \geq z_f\} \quad (4)$$

Cooling of T_{\perp} is termed geometrical cooling since it arises from the choice of coordinate system. By definition \hat{x}_{\perp} is perpendicular to the streamlines, and so as any atom moves further from the nozzle, its trajectory asymptotically approaches the streamlines and its component of velocity perpendicular to the streamlines asymptotically approaches zero.

Rather than dealing with a position-dependent T_{\perp} , it is preferable to deal with a measure of velocity spread that is independent of geometry. Virtual source radius r_v provides a suitable parameter. Atom-atom collisions within the continuum region randomize trajectories, causing the atom source to appear larger than the nozzle opening. If, in the free molecular flow region, atom trajectories were traced as straight lines back to the nozzle plane, the distribution of their intersection with the plane would describe this virtual source. The virtual source radius is defined as

$$r_v \equiv \frac{\Delta v_{\perp}(z)}{v_{\infty}} z \quad \{z \geq z_f\}, \quad (5)$$

where perpendicular velocity v_{\perp} is related to T_{\perp} by the usual

$$v_{\perp} = \sqrt{\frac{k_b T_{\perp}}{2m}}. \quad (6)$$

The expansion converts enthalpy to directed kinetic energy, so for a monatomic gas the terminal velocity v_{∞} is related to T_0 as¹⁶

$$v_{\infty} = \sqrt{\frac{5k_b T_0}{m}}. \quad (7)$$

Equation (5) may be interpreted as projecting a velocity distribution onto the nozzle plane. Cooling of T_{\perp} as z^{-2} ensures r_v is independent of geometry. Projecting the velocity back

from the freezing boundary or any point beyond produces the same value of r_v . Relations (3) through (7) can be combined to determine the dependence of the virtual source size on parallel speed ratio and nozzle diameter,

$$r_v \propto d \sqrt{S}. \quad (8)$$

For most monatomic gases, and for helium under stagnation conditions when quantum effects are not important, speed ratio is related to expansion strength as²

$$S \propto (P_0 d)^{1/2}, \quad (9)$$

implying

$$r_v \propto d^{5/4} P_0^{1/4}. \quad (10)$$

The most relevant implication of the above is that virtual source size grows faster than nozzle size and therefore faster than nozzle throughput. An improvement in brightness can be achieved through reduction in overall size of the experimental apparatus. For helium, the dependence of S on expansion strength is more complicated due to quantum effects on the scattering cross section² at low translational temperature. Quantum effects on r_v will be examined in the Sec. IV A of this article.

Although dependence on d and P_0 in relation (10) agrees with published data^{11,12,14,15} for Ar, Ne, and Kr, there is currently no theory which accurately predicts the magnitude of r_v ; this is why the above model is written in terms of a scaling argument rather than equalities. While accurate models for parallel speed ratio exist^{2,12} the difficulty working with perpendicular degrees of freedom is that T_{\perp} is far more sensitive to nonequilibrium effects. As the gas moves from equilibrium, T_{\perp} continues to cool while T_{\parallel} approaches its terminal value. Collisions therefore contribute a larger fractional energy change to perpendicular degrees of freedom than to the parallel degree of freedom.

Nonequilibrium, ($T_{\parallel} > T_{\perp}$), collisions cause strong deviation from a Maxwell-Boltzman perpendicular velocity distribution. The virtual source appears more as a sum of two sources; a small virtual source described by relation (10) for the central velocity distribution, and a larger, warmer, source for the broad tails of the distribution. Nonequilibrium collisions effectively remove atoms from the small source to the large source. Deviations from equilibrium, are already significant at only a few nozzle diameters from the source.² For a 1 μm nozzle diameter, atom-atom collisions are negligible on the length scale of a typical experimental apparatus, and so both virtual source radii are independent of nozzle-detector distance. As with the above model, the magnitude of r_v is determined by comparison to experiment.

B. Source brightness

The contribution to centerline intensity, I_0 , due to an area $dx dy$ at (x, y) in the virtual source plane is given by the brightness of the beam $B(x, y)$,

$$I_0 = \int B(x, y) dx dy \text{ (s sr)}^{-1}. \quad (11)$$

For a Gaussian virtual source $B(x, y)$ is given by

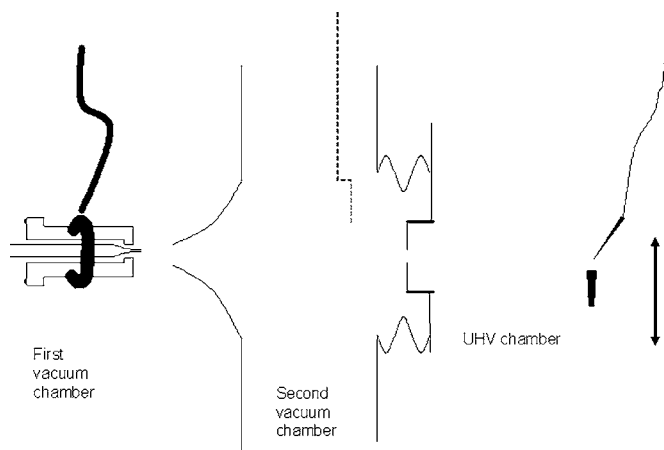


FIG. 1. The first chamber contains the nozzle and is separated from the second chamber by a $500\ \mu\text{m}$ skimmer. A movable flag (dashed) can be used to block the beam in front of the $2\ \mu\text{m}$ slit aperture. The UHV chamber connects to the second chamber by flexible bellows and contains the field ionization detector.

$$B(x,y) = \bar{B} \exp[-r^2/r_v^2] \text{ (s sr m}^2\text{)}^{-1}, \quad (12)$$

where

$$\bar{B} = \frac{I_0}{\pi r_v^2} \text{ (s sr m}^2\text{)}^{-1}. \quad (13)$$

That I_0 scales as the flux through the nozzle¹² $P_0 d^2$ along with relation (10) implies that \bar{B} scales as $(P_0/d)^{1/2}$. Small nozzle diameter and high stagnation pressure should therefore produce brighter sources. Moreover, depending on constraints such as the onset of cluster formation, pumping speed, and the impact of quantum effects on the scattering cross section, P_0 and d are normally inversely related so the impact on brightness of using smaller nozzles can be very significant. These constraints are discussed in Sec. IV.

III. EXPERIMENTAL SETUP

A. Vacuum system

A schematic of the experimental apparatus is shown in Fig. 1. The vacuum system consists of three chambers. The first chamber contains the nozzle and is pumped by a 7000 l/s diffusion pump which maintains pressure of about 10^{-6} torr for a $1\ \mu\text{m}$ nozzle at $P_0 = 10^4$ kPa. A 1500 l/s diffusion pump is connected to the second chamber through a baffle which prevents oil from entering this stage. The outlet of the smaller pump is connected to the first chamber, and so pressure in the first chamber is related to the total nozzle flux. These two chambers are connected through an electroformed skimmer 0.752 in. long with $500\ \mu\text{m}$ opening located 2 mm from the nozzle.

The third chamber is held at ultrahigh vacuum and houses the field ionization detector that is used for all our detailed beam measurements. This chamber is mounted on an optics table and is connected to the previous chamber by a flexible bellows. The beam enters this chamber through a $1.3\ \text{mm} \times 2\ \mu\text{m}$ collimating slit aperture affixed to the detector chamber 10.1 cm from the nozzle. This collimating aperture serves as a vacuum barrier permitting the chamber to be

kept at ultrahigh vacuum. An ion pump with a measured helium pumping speed of 33 l/s keeps the base pressure at 5×10^{-10} torr. The pressure level rises only by about 10^{-10} torr for a one micron nozzle at $P_0 = 10^4$ kPa. For alignment purposes, the detector chamber is permanently mounted on a linear motion stage that sits on a support made of three legs of adjustable height. The detector itself is connected through flexible bellows to external vertical and horizontal motion stages on the optics table. This arrangement allows alignment of the beam, collimator, and detector while operating under vacuum.

B. Detector

Helium atoms were field ionized¹⁷ in the field of a sharp tungsten tip at high voltage and the resulting ions were counted with a Galileo 4700 Channeltron channel electron multiplier and standard pulse counting electronics. The tungsten tip was prepared by ac electrochemical etch¹⁸ in a 1M solution of NaOH. For all measurements the tip was operated at the upper end of its working voltage range, 9 kV which corresponds to a surface field of about 6×10^{10} V/m. There was a gap of about 4 mm between the tip and the 1 cm cone of the multiplier. The tip was spot welded to a steel holder at a 71° angle to the beam axis and was cooled to prevent tungsten evaporation. The detector was located 19.4 cm from the nozzle. The field ionization tip detector is not pumped separately from the detector chamber, and we ionize background gas (mostly hydrogen) in that chamber as well as helium atoms in the beam. Elsewhere, we show¹⁹ that the tip has an ionization area of $\sim 0.007\ \mu\text{m}^2$ for a He beam at 77 K. Although the ionization area is nearly a factor 100 smaller for the directed flux than for diffuse background gas, this small ionization area geometrically favors the very small beam over the diffuse background gas. The background signal is typically ~ 1 Hz per 10^{-12} torr of background gas. By contrast, the helium flux in the beam corresponds to an effective pressure of order 10^{-6} torr and produces count rates of typically 1–10 kHz or 1–10 times larger than the background signal.

An image of the virtual source was formed by the slit aperture in similar manner to imaging of a pinhole camera only using a slit rather than pinhole. The image of the virtual source was recorded at the detector by scanning the field ionization tip through the image of the source in a direction perpendicular to the slit axis. The error in alignment between the slit and horizontal axis of the detector was 1.2° . The computer controlled detector stage can move with $0.1\ \mu\text{m}$ resolution over a 5 mm range, however, scans were taken over a range smaller than 5 mm and depending on the size of the image. The virtual source images deviate considerably from Gaussian and contain a broad thin tail which is difficult to discern from the background. After careful analysis of the data it was found that most of the scans were taken over a range smaller than that for which some signal could still be distinguished from the background. For consistency during analysis, only data out to a standard measure from the central axis was used. This measure was chosen as four times width at half maximum. Comparison to the broadest scans taken,

showed this truncation resulted in an error on r_v that depended on nozzle, but was generally less than 10%.

C. Nozzles

Nozzles were made from 1.2 mm o.d. \times 0.69 mm i.d. borosilicate capillary tubes commonly used in neuroscience as patch clamps, and more recently finding application as microskimmers.²⁰ A laser-based micropipette puller from Sutter Instrument Co. made converging nozzles with diameters up to 5 μm easily and reproducibly. Larger openings require some luck or patience to produce. 0.5 μm nozzles were the smallest used for this experiment, but smaller nozzles can be made by the method of pressure polishing.²¹ Glass nozzle diameters studied were 0.63, 0.75, 1.2, 1.8, and 4.3 μm .

Nozzles were held in commercially available, blank, face seal, stainless-steel fittings that were drilled out to accommodate a glass tube. Nozzles were held in place with a drop of epoxy. In the vacuum chamber, nozzle assemblies were held in a cold finger, which could be cooled to 77 K. The cold finger was mounted on an XYZ stage to allow alignment of the nozzle and skimmer.

Nozzles were also made by welding commercially available apertures to VCR sockets. The apertures purchased from National Aperture were laser drilled in stainless steel foil. The steel foil was 12.5 μm thick, making the 2–5 μm apertures more resemble tubes than sharp-edged orifices. To assemble the nozzle, the foil was first clamped between the VCR fitting and a center-drilled disk. All three pieces were then welded together. Steel nozzle diameters studied in were 2.4, 6.3, and 9.3 μm .

Contaminates in the helium and gas lines were initially a problem. To avoid clogging by particulates, all gas lines were cleaned with HCl, water, acetone, and isopropyl alcohol in that order. Different grades of helium were tried and Air Products BIP brand with advertised THC < 100 ppb (parts per billion) was found to be suitable for all nozzle sizes. A liquid-nitrogen-cooled filter was used as a to remove condensable gases, but may not be necessary. Once all lines were cleaned and baked under vacuum after any exposure to air, clogging was no longer a problem. Steel nozzles presented an additional problem with 2 μm steel nozzles only becoming reliable when all pieces of the nozzle assembly were electro polished before being welded together.

Both glass and steel nozzle diameters were determined through source chamber pressure measurements. All nozzles were operated at Reynolds number of 100 or greater to minimize viscous effects on effective nozzle diameter.

IV. RESULTS

A. Virtual source size

Representative images of the virtual source, using the 4.3 μm diameter glass capillary nozzle at $T_0=300$ K and $P_0=4 \times 10^3$ kPa are shown in Fig. 2. Four different model functions of cylindrical symmetry plus constant backgrounds were used to fit the virtual source images using a weighted least-squares fit. The model distributions were integrated over one Cartesian coordinate since the slit was always much

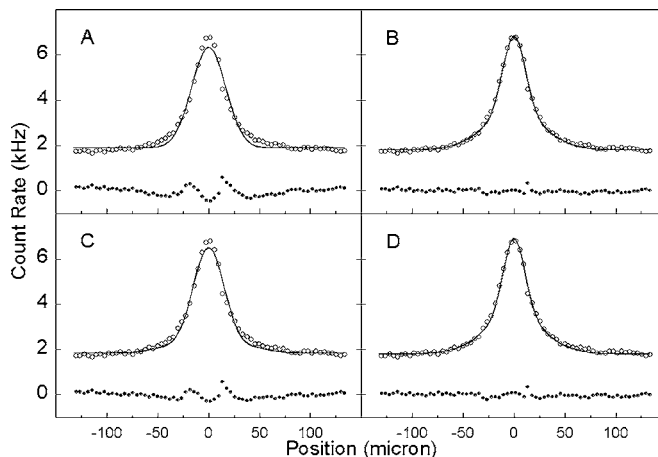


FIG. 2. Four different fits to data and residual for a 4.3 μm diameter nozzle at 300 K and 4×10^3 kPa. Single Maxwell-Boltzmann (MB) fit (A), two MB fit (B), single MB with a deformation (C), and two MB fit with deformation applied to smaller source (D).

longer than the virtual source. The distributions were also convoluted with a rectangular function to take account of the finite width of the slit. This convolution was relevant for only the smallest nozzles at low stagnation P_0 . At large throughput, the ion pump produced a nonuniform background of ions in the chamber that needed to be added to the constant background in the fit for the cold 6.3 and 9.3 μm diameter nozzles.

In the two-source fit, Fig. 2(b), a second Maxwell-Boltzmann distribution is added to fit the broad wing of the distribution caused by nonequilibrium effects as discussed above,

$$B(r) = \bar{B}_1 \cdot g(r/r_{v1}) + \bar{B}_2 \cdot g(r/r_{v2}). \quad (14)$$

Virtual source radii are given by r_2 and r_1 and $g(r/r_i)$ are Gaussian distributions of brightness B_1 and B_2 . Also shown in Fig. 2(c) is a fit to a single deformed Gaussian as given by the following equation by Klots:²²

$$B(r) = \bar{B} \cdot g(r/r_v) \{1 + \gamma \cdot L_2[(r/r_v)^2]\}. \quad (15)$$

Here the Maxwell-Boltzmann distribution is deformed by L_2 , the second Laguerre polynomial, which roughly has the effect of redistributing intensity to the wings of the distribution. Five measurements of the “kurtosis parameter” γ were made for nozzles at 4×10^3 kPa with an average 0.52 ± 0.05 . Using the position of the freezing surface as determined by Beijernick *et al.*,¹⁴ one can extract a value of $\gamma=0.85$ from Klots theory.²² Yet another fit shown in Fig. 2(d) with the addition of a second Gaussian to the right-hand side of Eq. (15) as was done^{14,15} by the Eindhoven group.

While the difference between a single Gaussian and deformed Gaussian was significant, the difference between two-Gaussian and deformed two-Gaussian was negligible at the resolution of these scans. The residuals for all four fits are shown in Fig. 2. The two-Gaussian fit was considered satisfactory without a deformation term and was used for all data presented in this paper.

Our measurements of the two Gaussian virtual source sizes are shown in Fig. 3 for nozzles at $T_0=300$ K. Included

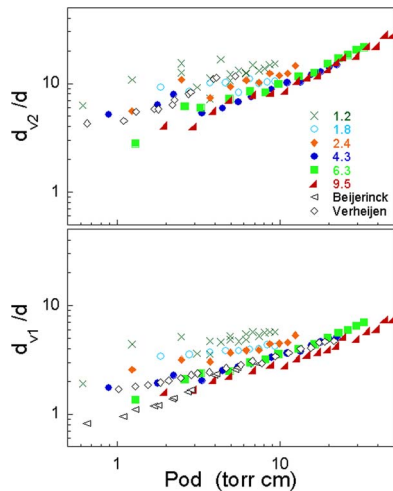


FIG. 3. Large (upper) and small (lower) virtual source size given as virtual source diameter divided by nozzle diameter at 300 K. Data of Verheijen *et al.* $d=94\text{ }\mu\text{m}$ and data of Beijerinck *et al.* $d=50\text{ }\mu\text{m}$ are displayed for comparison; both include a deformation term.

for comparison are results from two previous studies published by others,^{14,15} both of which use a deformed two-Gaussian fit. The data from Beijerinck used a constant radius r_2 for the larger distribution due to difficulty resolving the tails of the distribution. We do not present our data for the 0.63 and 0.75 μm diameter nozzles at 300 K as insufficient resolution was used during data collection. Results are displayed as scaled virtual source size d_{vi}/d where the d_{vi} are just twice the virtual source radii. Equation (10) can be scaled similarly,

$$d_v/d \propto (dP_0)^{1/4}. \tag{16}$$

For comparison to the data of others,^{12,14,15} we try an empirical fit as shown below,

$$d_{v1}/d = a(dP_0)^\alpha. \tag{17}$$

Derived values of a and α for all plots in Fig. 3 are displayed in Table I. To compare different nozzles, the same range of P_0d from 2 to 10 torr cm was analyzed for each nozzle. The exponent α increases with nozzle size leaving two possibilities; the scaled virtual source size d_{vi}/d is not a unique function of P_0d or quantum effects are relevant and more strongly influence the large nozzles. If this is the result of

TABLE I. A comparison for various nozzle sizes for the same range of expansion strength $2 < P_0d < 10$. A fit of $d_{v1}/d = a(P_0d)^\alpha$ shows increasing α with nozzle size.

	Nozzle diameter	Exponent	α	Coefficient a
	1.2	0.11	4.4	
	1.8	0.15	3.0	
	2.4	0.27	2.3	
	4.3	0.32	1.6	
	6.3	0.36	1.5	
	9.5	0.45	1.1	
Beijerinck <i>et al.</i> ^a	50	0.31	1.6	
Verheijen <i>et al.</i> ^b	94	0.64	0.87	

^aUsed constant $d_{v2}/d=20$.
^bUsed deformation on smaller source.

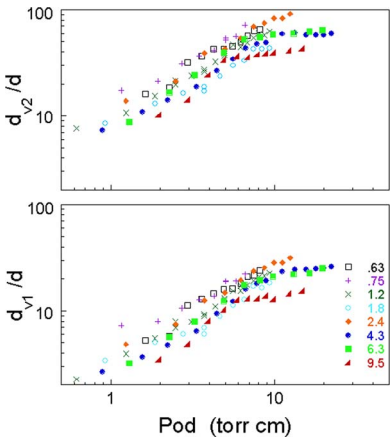


FIG. 4. Large (upper) and small (lower) virtual source diameter divided by nozzle diameter at 77 K.

quantum effects it would be at a lower P_0d than expected. For the parallel speed ratio, quantum effects become strong² at about 20 torr cm at $T_0=300\text{ K}$ and 2 torr cm at $T_0=77\text{ K}$.

Quantum effects are apparent in Fig. 4, which shows virtual source sizes $T_0=77\text{ K}$. In the classical regime, $P_0d < 2$ torr cm, r_v grows slowly with P_0d . In the quantum regime, $P_0d > 2$ torr cm, r_v initially grows rapidly with P_0d between 2 and 9 torr cm due to a rapid increase in He–He scattering cross section and then begins to level off above 9 torr cm. Data for the 4.3 μm diameter nozzle shows all three of these features and is reproduced in Fig. 5. To date there is no other data for comparison on virtual source size for nozzle conditions at which quantum effects are strong.

A theoretical model for virtual source size including quantum effects is not available so the following crude but simple method is used. Combining relations (8), (9), and (17), we predict

$$d_{v1}/d = aS^{2\alpha}. \tag{18}$$

Values for a and α of 0.80 and 0.26, respectively, were taken from the semiempirical thermal conduction model¹² for a monatomic gas. Quantum effects are included using published numbers for parallel speed ratio.² The results are shown as the solid line in Fig. 5. We see that this simple hybrid model predicts the virtual source size to within a factor of order unity. These results indicate that quantum effects which decrease the parallel velocity spread simultaneously increase the perpendicular velocity spread.

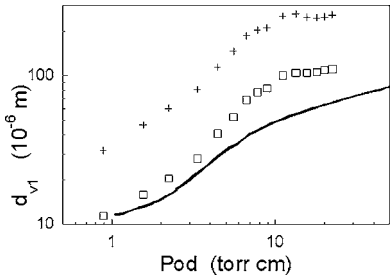


FIG. 5. Large and small virtual source for 4.3 μm 77 K nozzle compared to model (solid line).

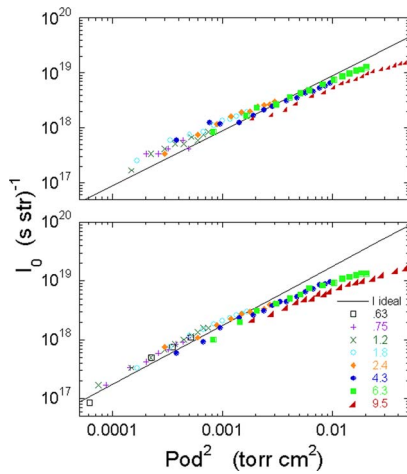


FIG. 6. Intensity vs $P_0 d^2$ data for several nozzle sizes at 300 K (upper) and 77 K (lower) reservoir temperature. The solid line is theory.

B. Intensity

Pressure readings corrected for He, combined with the measured pumping speed in the UHV chamber were used to calculate centerline intensity. To ensure that measured pressure differences were entirely due to directed and not effusive flow, the pressure in the chamber was measured with and without the beam blocked by a movable flag mounted between the UHV chamber and source chamber. Intensity data are shown for $T_0=77$ and 300 K in Fig. 6 and are compared to ideal intensity,¹²

$$I_0 = 0.36 P_0 d^2 (m k_b T_0)^{-1/2}. \quad (19)$$

Figure 6 shows that intensity increases with increasing nozzle throughput, which is proportional to $P_0 d^2$, but the rate at which intensity grows is less than ideal for the highest measured throughput values. At high $P_0 d^2$, pressure in the first two vacuum chambers grows linearly, but pressure in the UHV chamber does not, implying that the attenuation is caused by scattering off the background gas near the collimating slit.

Removing the skimmer results in a higher attenuation by scattering off the background gas. The effect on intensity of removing the skimmer has been examined in the same apparatus using the 2.4 μm nozzle and with a 200 μm aperture in place of the slit aperture. Intensity was attenuated by 30% at stagnation pressure of 7000 kPa and 10% and 3000 kPa. Submicron nozzles therefore likely do not require skimmers. The skimmer does nevertheless serve a useful purpose in the apparatus described in this paper; it prevents diffusion pump oil from coating the collimating slit.

The intensity contribution of the small virtual source I_1 is shown in Fig. 7. For the warm nozzles, the small source intensity is between 0.5 and 0.75 of the total intensity I_0 with smaller nozzles showing larger values of I_1 . For the cold nozzles this ratio is between 0.25 and one half. The individual source intensities provide a measure of the deviation from a single Maxwell-Boltzman source with low values of I_1 representing more small angle scattering into the broader distribution. Quantum effects are relevant for the cold source and, as is true for the parallel distribution,²³ appear to cause

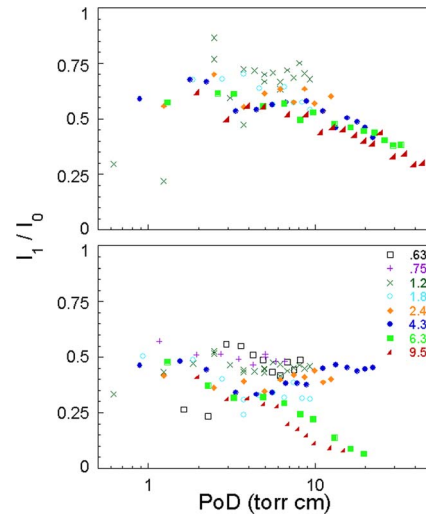


FIG. 7. Fraction of intensity in the smaller virtual source for 300 K (upper) and 77 K (lower) nozzles.

stronger deviation from the central distribution.

Two anomalies are present in Fig. 7. At $P_0 d$ above 10 torr cm, the warm nozzles show a sharp decrease in I_1 fraction. As in the previous section this suggests the perpendicular velocity distribution is sensitive to quantum effects at lowers value of $P_0 d$ than is the parallel distribution. The second surprise is that at high nozzle flux values, or high $P_0 d$ for the cold 6.3 and 9.5 μm nozzles, there appears to be an unusually small fraction of intensity associated with the smaller virtual source. It is likely this may be a problem with the fitting routine; the fit for only the cold 9.5 and 6.3 μm diameter nozzles included an extra background term for ion pump noise adding some difficulty in finding a stable minimum. Condensation may also be a factor. Parallel speed ratio has been show to decrease beyond the onset of helium trimer formation at $P_0 d=20$ torr cm and 80 K for a 5 μm nozzle.²⁴

C. Brightness

Average brightness \bar{B} of the sources as defined in Eq. (13) are shown as a function of $P_0 d$ in Figs. 8 and 9. Virtual source scan count rates were converted to average brightness by comparison to intensity measurements. The smaller nozzles are consistently brighter at both temperatures, in line with the sudden freeze model discussed in Sec. II. At $T_0=300$ K, \bar{B} initially increases with pressure then drops at high flux values. This drop is a result of both the attenuation of intensity at high flux as described in Sec. IV B and the growth of the virtual source for large nozzles as described in the previous section. At $T_0=77$ K, \bar{B} peaks around 2 torr cm then drops due to the rapid increase in r_v due to the onset of quantum effects. Our 300 K beam brightness results in the classical regime are close to the values one would expect from extrapolating the published data of the Eindhoven group for I_0 and r_v to smaller nozzle diameter. As for the quantum regime, no other brightness data is available for comparison.

Combining Eqs. (13), (18), and (19) with $a=0.80$ and $\alpha=0.26$ gives

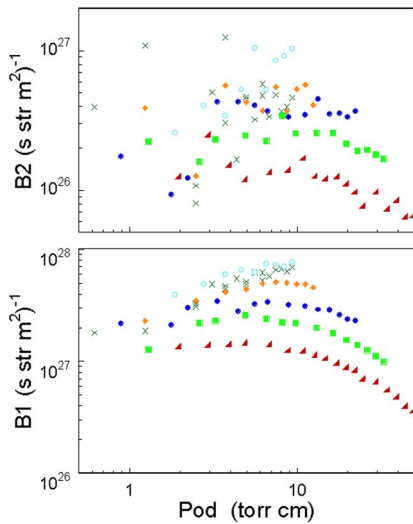


FIG. 8. \bar{B}_i values for large and small virtual source at 300 K nozzle temperature.

$$\bar{B}_1 = 0.18 \frac{P_0}{S(mk_b T_0)^{1/2}}, \quad (20)$$

where I_1 was taken to be approximately half the total intensity. Using published speed ratio numbers² again to predict virtual source area it would appear that the growth in scattering cross section should level off for $P_0 d > 9$ torr cm and \bar{B} should again increase, achieving nearly the same brightness (with lower energy bandwidth) at 50 torr cm as it does at 2 torr cm. In Fig. 9 the 4.3 and 2.4 μm diameter nozzles both increase in brightness above 9 torr cm, but with the 6.3 and 9.5 μm diameter nozzles \bar{B}_1 decreases while \bar{B}_2 increases. This result is due to the decrease in intensity I_1 as discussed in the previous section.

At this point it should be mentioned that a commonly used measure in fields that work with coherence is spectral brightness. Spectral brightness, the brightness per bandwidth of the source in $(\text{s sr m}^2 \Delta\nu)^{-1}$ scales as the product of

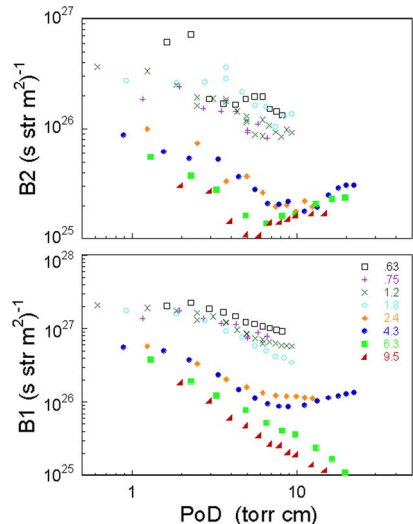


FIG. 9. \bar{B}_i values for large and small virtual source at 77 K nozzle temperature.

brightness and speed ratio and therefore is not diminished by quantum effects.

D. Coherent flux

The dependence of the transverse coherent flux, F_c , on P_0 and d is the same as that for \bar{B} as implied by Eq. (2) (reproduced below),

$$F_c = 0.063 \bar{B} \lambda^2. \quad (2')$$

Temperature dependence of F_c , however, enters not only through \bar{B} , but also on the de Broglie wavelength λ ,

$$\lambda = \frac{h}{(5mk_b T_0)^{1/2}}. \quad (21)$$

For any given nozzle size, the peak brightness for T_0 of 300 and 77 K using Eq. (20) occurs at $P_0 d$ of 40 and 2 torr cm, respectively. The peak coherent flux at 300 K is expected to be a factor 2.6 larger than the peak coherent flux at 77 K but it comes at a high price, a higher gas load, and increased pumping requirement due to the factor of 20 higher stagnation pressure.

As an example, consider the 1.2 μm diameter nozzle, which is the smallest nozzle for which brightness data are available at 300 K. From Eq. (21), $\lambda = 0.56$ and 1.1 \AA at 300 and 77 K, respectively. The choice of \bar{B}_1 or \bar{B}_2 in Eq. (2') for F_c depends on the experimental setup. If a two-aperture collimator is used then the coherence properties are defined by the collimator and \bar{B}_1 may be used to calculate F_c . Figure 8 shows \bar{B}_1 is $7.1 \times 10^{27} (\text{s sr m}^2)^{-1}$ at 300 K and $P_0 d = 9.3$ torr cm which corresponds to $F_c = 1.4 \times 10^6 \text{ s}^{-1}$. At 77 K and $P_0 d = 2.5$ torr cm \bar{B}_1 is $1.4 \times 10^{27} (\text{s sr m}^2)^{-1}$ corresponding to $F_c = 1.1 \times 10^6 \text{ s}^{-1}$. Without using a collimator, it is the large virtual source which defines the transverse coherence. Using \bar{B}_2 results in a smaller F_c on the order of 10^5 s^{-1} .

V. DISCUSSION

Small nozzles provide an easy and relatively inexpensive way to produce a high brightness free jet helium atom source. Nozzles of submicron diameter are routinely made from glass capillary tubing. Gas load scales as $P_0 d^2$, which means that vacuum apparatus using such small nozzles has only a moderate demand for pumping speed. There is no tradeoff between pumping speed and brightness when considering nozzle size; reducing nozzle size also increases brightness.

High brightness beams should not be thought of as a replacement for high intensity beams but rather as a tool for any application requiring a highly collimated or spatially filtered beam such as DAS and atom microscopy. While it appears somewhat nonintuitive that in certain applications more signal can be obtained by using smaller nozzles, this appears to be the case. The virtual source images taken for this report are an example of a study that benefits from high brightness. Despite the wide range of nozzle size used, a factor of more than two orders of magnitude nozzle area, the signal ranged only over a factor order unity.

The design of future generation high brightness apparatus depends on the desired parallel speed ratio. There is a

tradeoff between longitudinal and transverse coherence. The high parallel speed ratio which can be obtained using helium comes with a sharp decrease in brightness as P_0d enters the quantum regime. High brightness designs can be classified as either a large apparatus, operating with P_0d well into the quantum regime, or small systems operating just below the quantum regime where the helium behaves as a classical expansion.

In the case of a large system operating at high S_{\parallel} it may be possible to obtain brightness comparable to that in the classical regime by operating at high pressure. This requires considerable pumping speed. Even with our 7000 l/s diffusion pump, at values of P_0d well into the quantum regime, scattering off the background gas diminished the centerline intensity to the point where we were unable to obtain the predicted similar values of brightness as found just below the quantum regime. Such a system must also be operated below condensation limit which may be difficult at best. Other gases may have an advantage over helium for a system with these requirements. Without quantum effects, brightness is expected to scale as $B \propto \sqrt{P_0/d}$, and speed ratio as $S_{\parallel} \propto \sqrt{P_0d}$ and so a compromise may be obtained at high pressure.

For applications with a lower demand on parallel speed ratio, the apparatus can be made much smaller. As an example of a system based on a small nozzle, consider a 0.2 μm diameter nozzle operating just below the onset of the quantum effects at $P_0 = 13 \text{ MPa}$ and $T_0 = 77 \text{ K}$. Such a source would have very high brightness and small demands on pumping speed. Extrapolating the data from the previous section, B_1 would be $3 \times 10^{28} (\text{s sr m}^2)^{-1}$ and virtual source diameter $d_{v1} \cong 0.7 \mu\text{m}$. This brightness is, for example, comparable to modern x-ray undulators at third generation synchrotron radiation facilities. The throughput would be small enough that a source chamber pressure of 10^{-5} torr could be maintained using a 350 l/s pump, within the range of a compact turbomolecular pump. Using a turbo pump instead of a diffusion pump means that there will be no oil in the source chamber, thereby eliminating the need of a skimmer to shield filtering apertures and also eliminating another stage of pumping and allowing a still more compact apparatus.

ACKNOWLEDGMENTS

We gratefully acknowledge financial support from the National Science Foundation under Grant No. DMR-0079584. We thank Greg Elliot for many useful discussions.

- ¹R. Campargue, A. Lebehot, and J. C. Lemonnier, 10th International Symposium on Rarefied Gas Dynamics, 1033 (1976); L. Pedemonte, G. Bracco, and R. Tatarek, Phys. Rev. A **59**, 3084 (1999).
- ²J. Peter Toennies and K. Winkelmann, J. Chem. Phys. **66**, 3965 (1977).
- ³E. Hulpke, *Helium Atom Scattering from Surfaces* (Springer, Berlin, 1992), p. 323; L. Pedemonte, A. Gussoni, R. Tatarek, and G. Bracco, Rev. Sci. Instrum. **73**, 4257 (2002).
- ⁴B. Chu, *Dynamic Laser Light Scattering* (Academic, San Diego, 1991).
- ⁵J. Miao, P. Charalambous, J. Kirz, and D. Sayre, Nature (London) **400**, 342 (1999); D. T. Attwood, *Soft X-Rays and Extreme Ultraviolet Radiation* (Cambridge University Press, Cambridge, 2000); S. Eisebitt, J. Lüning, W. F. Schlöter, M. Lörger, O. Hellwig, W. Eberhardt, and J. Stöhr, Nature (London) **432**, 885 (2004); M. S. Pierce, R. G. Moore, L. B. Sorensen, S. D. Kevan, O. Hellwig, E. E. Fullerton, and J. B. Kortright, Phys. Rev. Lett. **90**, 175502 (2003); Y.-S. Seo, T. Koga, J. Sokolov, M. H. Rafailovich, M. Tolan, and S. K. Sinha, Phys. Rev. Lett. **94**, 157802 (2005).
- ⁶M. Born and E. Wolf, *Principles of Optics: Electromagnetic Theory of Propagation, Interference and Diffraction of Light*, sixth ed. (Pergamon, Oxford/New York, 1980).
- ⁷J. B. Anderson and J. B. Fenn, Phys. Fluids **8**, 780 (1965).
- ⁸E. P. Muntz, 5th International Symposium on Rarefied Gas Dynamics, Vol. 2, 1257 (1966); N. Abuaf, J. B. Anderson, R. P. Andres, J. B. Fenn, and D. R. Miller, 5th International Symposium on Rarefied Gas Dynamics, Vol. 2 (1966).
- ⁹B. B. Hamel and D. R. Willis, Phys. Fluids **9**, 829 (1966); R. H. Edwards and H. K. Cheng, 5th International Symposium on Rarefied Gas Dynamics, Vol. 1, 819 (1966).
- ¹⁰D. R. Willis, B. B. Hamel, and J. T. Lin, Phys. Fluids **15**, 573 (1972); A. U Chatwani, 10th International Symposium on Rarefied Gas Dynamics, Vol. 51, Part 1, 461 (1976).
- ¹¹A. H. M. Habets, H. C. W. Beijerinck, M. J. Verheijen, and J. P. L. M. N. de Warrimont, 10th International Symposium on Rarefied Gas Dynamics, Vol. 51, Part 2, 919 (1976).
- ¹²H. C. W. Beijerinck and N. F. Verster, Physica B & C **111**, 327 (1981).
- ¹³C. E. Klots, J. Chem. Phys. **72**, 192 (1980).
- ¹⁴H. C. W. Beijerinck, G. H. Kaashoek, J. P. M. Beijers, and M. J. Verheijen, Physica B & C **121**, 425 (1983).
- ¹⁵M. J. Verheijen, H. C. W. Beijerinck, W. A. Renes, and N. F. Verster, J. Phys. E **17**, 1207 (1984).
- ¹⁶G. Scoles, *Atomic and Molecular Beam Methods* (Oxford University Press, New York, 1988), Vol. 1.
- ¹⁷E. W. Muller, in *Advances in Electronics and Electron Physics*, edited by L. Marton (Academic, New York, 1960), Vol. XIII, pp. 83; R. B. Doak, Y. Ekinici, B. Holst, J. P. Toennies, T. Al-Kassab, and A. Heinrich, Rev. Sci. Instrum. **75**, 405 (2004).
- ¹⁸W. P. Dyke, J. K. Trolan, W. W. Dolan, and G. Barnes, J. Appl. Phys. **24**, 570 (1953).
- ¹⁹D. P. DePonte, S. D. Kevan, and G. S. Elliott, Rev. Sci. Instrum. (submitted).
- ²⁰J. Braun, P. K. Day, J. P. Toennies, G. Witte, and E. Neher, Rev. Sci. Instrum. **68**, 3001 (1997).
- ²¹M. B. Goodman and S. R. Lockery, J. Neurosci. Methods **100**, 13 (2000).
- ²²C. E. Klots, Chem. Phys. **67**, 75 (1982).
- ²³G. Brusdeylins, H. D. Meyer, J. P. Toennies, and K. Winkelmann, 10th International Symposium on Rarefied Gas Dynamics, Vol. 51, Part 2, 1047 (1976).
- ²⁴L. W. Bruch, W. Schollkopf, and J. Peter Toennies, J. Chem. Phys. **117**, 1544 (2002).